research papers

ID22: a multitechnique hard X-ray microprobe beamline at the European Synchrotron Radiation Facility

A. Somogyi,[a]*‡ R. Tucoulou,[a] G. Martinez-Criado,[a] A. Homs,[a] J. Cauzid,[a,b] P. Bleuet,[a] S. Bohic[a] and A. Simionovici[a,c]

[a]ID22, European Synchrotron Radiation Facility, BP220, 38043 Grenoble CEDEX, France, [b]Institut de Physique du Globe de Paris, Jussieu, 75252 Paris CEDEX 05, France, and [c]École Normal Supérieure, Lyon, France. E-mail: somogyi@synchrotron-soleil.fr

The ID22 beamline is dedicated to hard X-ray microanalysis allowing the combination of fluorescence, spectroscopy, diffraction and tomography techniques in a wide energy range from 6 to 70 keV. The recent installation of an in-vacuum undulator, a new sample stage and the adaptation of various focusing optics has contributed to a great improvement in the capabilities of the beamline, which is now accessed by a wide user community issued from medical, earth and environmental science, archaeology and material science. Many applications requiring low detection limits for localization/speciation of trace elements together with structural analysis have been developed at the beamline on the (sub)micrometer scale. The possibility of combining simultaneously different analytical probes offers the opportunity of a thorough study of a given sample or scientific problem. This paper presents a review of the recent developments of the beamline and a detailed description of its capabilities through examples from different fields of applications.

1. Introduction

The possibility of obtaining simultaneous information about diverse sample characteristics such as morphology, crystalline structure, quantitative internal elemental composition and chemical speciation at trace-element levels (ppm) in a non-destructive manner is a general requirement of several research fields such as biology, material science, environmental science, geology and archaeology. The *in situ* evaluation of different chemical, physical and environmental processes often requires the study of the spatial variation of the various sample characteristics with high-(sub)micrometer resolution as a valuable complement to the average bulk information. Obtaining micrometer-scale information is often the only possible method of checking and developing the theoretical models of the different processes, providing a possibility for the prediction and/or modification of their effects or consequences.

The increasing number of synchrotron beamlines providing (sub)microanalytical techniques answers the growing demand for microanalytical investigations. Although several of them provide more than one experimental technique, still only few

‡ Recent address: DiffAbs BL, Synchrotron Soleil, BP 48, Saint-Aubin, 91192 Gif-sur-Yvette CEDEX, France.

facilities can offer the combined use of various microanalytical methods on a routine basis (Marcus *et al.*, 2004; Newville *et al.*, 1999; Sutton *et al.*, 2004). The ID22 beamline of the European Synchrotron Radiation Facility (ESRF) is dedicated to hard X-ray microanalysis in the 6–70 keV energy range allowing for the combination of micro-X-ray fluorescence (μ-XRF), micro-X-ray absorption (μ-XAS), micro-X-ray diffraction (μ-XRD) and XRF/absorption/phase-contrast tomography. The recent upgrade of the beamline aims to fulfil the requirements for a reproducible, fast and flexible combination of these analytical techniques offering partial online data-treatment capabilities for the user community. The use of different focusing devices opens the possibility of covering the full available energy range while adapting the focal spot size to the experimental needs.

2. Beamline description

2.1. X-ray source

The ID22 beamline is installed at a high-β straight section equipped with two different undulators. The U42 standard linear undulator (minimum gap 16 mm) covers the 6–50 keV energy range (the low-energy limit is imposed by the

absorption within the Be windows and air). The magnets of the U23 in-vacuum linear undulator are situated inside the vacuum vessel of the storage ring. The gap can therefore be closed to smaller values (>6 mm) inducing an important gain in brilliance also for the higher harmonics of the undulator spectrum up to 70 keV. Calculations [using the *SRWE* program (Chubar & Elleaume, 1998)] show that the brilliance is higher than 10^{19} photons s^{-1} (0.1% bandwidth)$^{-1}$ mrad^{-2} mm^{-2} (200 mA) in the 7–14 keV and 21–70 keV energy ranges and a little lower in the 14–21 keV range (see Fig. 1). The two undulators can also be used simultaneously.

2.2. Optics hutch

The optical layout of the beamline is composed of several pairs of slits, a flat vertical mirror and a monochromator. The optical elements are moveable in such a way that any of the various beam modes (white, pink, monochromatic, monochromatic + reflected) can reach the experimental hutch.
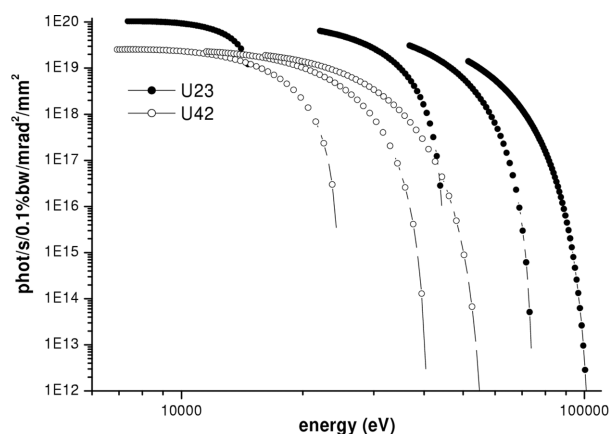

Figure 1
Brilliance of the U23 and U42 undulators of the ID22 beamline calculated using the *SRWE* software. The calculations do not take into account the absorption within the front-end diamond window and Be windows.
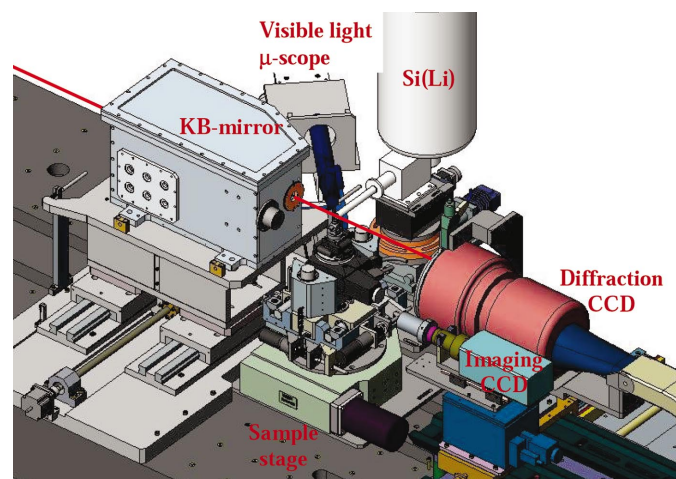

Figure 2
Sketch of the ID22 microprobe set-up.

The role of the first optical element of the beamline, a flat horizontally deflecting Si mirror, is twofold: as a low-pass filter it reduces the higher harmonic content of the X-ray beam and moderates the heat load on the monochromator crystals. The Si crystal itself and two different coatings, Pd and Pt, are available for choosing the cut-off energy of the primary beam. The incident angle can be changed between 2.26 and 2.6 mrad defining the cut-off energies of the Si, Pd or Pt stripes in the ranges 12–14 keV, 24–25 keV and 32–37 keV, respectively. The large 850 mm mirror length ensures that the full horizontal beam size is accepted by the mirror within this angular range.

A Kohzu fixed-exit double-crystal monochromator is used in the 3–33° angular range with two different pairs of crystals: Si(111) to reach the 6–33 keV energy range and Si(311) with higher-energy resolution up to 65 keV. Each first crystal is cooled by a closed liquid-nitrogen cryo-loop.

2.3. Microprobe set-up

The microprobe set-up (see Fig. 2) is installed in the first experimental hutch on a moveable granite table, which can be aligned horizontally and vertically with ∼5 μm reproducibility depending on the used beam mode (monochromatic/pink/white). The focusing optics is usually situated at ∼41 m from the X-ray source. Different focusing devices (Kirkpatrick–Baez mirror at $E < 18$ keV; compound refractive lens at $E > 18$ keV) are used for efficient focusing in the available 6–70 keV energy range.

2.3.1. Focusing optics. For achromatic focusing in the 6–18 keV energy range, a perpendicularly crossed elliptical Rh-coated mirror-pair in the Kirkpatrick–Baez (KB) geometry was designed and mounted by the ESRF optics group (Hignette *et al.*, 2001) in 2002. The KB mirror-pair is enclosed in a He chamber to protect the mirrors from chemical surface damage and to ensure their thermal stability. The acceptances of the horizontal and vertical mirrors at a nominal incident angle of 3.5 mrad are 0.25 mm and 0.4 mm, respectively. In the specific case of higher-energy application (up to 30 keV), the glancing angle on the mirrors can be decreased to 2 mrad. The respective nominal focal distances are 190 mm and 390 mm from the middles of the horizontally and vertically focusing mirrors, respectively. This relatively large working distance has been chosen to ensure enough free space around the sample for the installation of beam monitors and various sample environments, *e.g.* high-pressure cell, He/vacuum sample chamber.

Since the X-ray source is strongly asymmetric, the horizontal and vertical dimensions of the focal spot are not determined by the same optical principle. Owing to the large (∼800 μm FWHM) horizontal source size the horizontal spot size can be deduced by the geometrical demagnification factor (0.19 m/41 m), giving a FWHM of ∼3.5 μm. The vertical spot size, on the other hand, should be determined by the slope error of the vertically focusing mirror (0.34 μrad r.m.s. after shaping). Using the knife-edge technique, the measured spot-size values are 3.5 μm (H) × 0.8–1 μm (V) with a depth of focus of ∼300 μm. The photon flux measured in the focal spot

is between 10^{11} and 10^{12} photons s^{-1} (200 mA)$^{-1}$ corresponding to $\sim$70% efficiency of both KB mirrors.

Owing to the low divergence of the high-β source, a submicrometer horizontal spot size of relatively high intensity can still be achieved by creating a small ($<$100 µm) secondary horizontal source by closing the primary slit situated at $\sim$21 m from the focusing device. A horizontal focal spot of 0.65 µm with $\sim$10^{10} photons s^{-1} photon flux can be obtained at 12 keV energy using a 50 µm horizontal slit size.

The stability of the focal spot position and size is an essential issue for microanalysis. While changing the energy of the X-ray beam in the 8–18 keV range the position of the focal spot changes by less than 2 µm in both directions.

The low-frequency stability of the mirror bendings has been characterized by regular spot-size measurements. In the uniform filling mode of the ring (most stable e^{-} beam) the spot size does not show any significant change over the period of a standard user experiment (a few days). The angular beam stability upstream of the KB mirrors is a key parameter for the stability of the spatial resolution of the microprobe: a 1 µrad glancing angle variation on any mirror results in a significant focal spot movement at the sample position (e.g. 0.4 µm vertically). Beam monitoring and active feedback, which seem to be essential to control and maintain the long-term spatial resolution, is planned to be implemented in the future.

The KB optics is mounted onto a motorized horizontal translation stage and can be positioned with $<$1 µrad reproducibility without significant change of the position ($<$1 µm) and size ($<$10%) of the focused beam into and out of the beam. The easy KB movement makes the combination of full-field imaging (absorption/phase-contrast imaging and tomography) and other microanalysis techniques possible. It also provides an opportunity for an easy, rapid and reproducible switch between various focusing optics covering different energy ranges or providing different spot sizes during a user experiment.

At energies above 18 keV, Al parabolic compound refractive lenses (CRL) are used as focusing optics (Lengeler et al., 2002). Although CRL lenses are chromatic focusing devices and their 1–2% efficiency is small compared with that of the KB system, they have several advantages: they are in-line focusing elements, they do not destroy the coherence of the synchrotron beam and they are easy to align compared with the KB mirror.

The size of the demagnified source depends on the number of individual lenses used (through the focal distance). It is typically 1–2 µm vertically and 12–15 µm horizontally corresponding to a 0.5–2 m focal distance with a photon flux of $\sim$10^{10} photons s^{-1}. Smaller spot sizes can be reached by using more lenses at the expense of beam intensity owing to the larger absorption in the lens material. The dimensions of the horizontal spot size can be reduced by creating a small horizontal secondary source as mentioned above.

Other types of focusing devices successfully tested at the beamline and providing higher efficiency and/or submicrometer spot size, e.g. Be lenses (Lengeler et al., 2004), linear Si lenses (Schroer et al., 2003), SU8 lenses (Nazmov et al., 2004) and diffractive lenses (David et al., 2001), are also intended to be used routinely in the near future.

2.3.2. Sample stage. The sample stage has been designed and optimized to perform microfluorescence/absorption/diffraction mappings and XRF-, absorption and phase-contrast-tomography measurements on a wide variety of samples in an in situ environment. It allows the accommodation of various types of standard sample holders such as films or capillaries, but also high-pressure cells, small vacuum or Helium chambers and piezo stage. In order to make possible the measurement of the very same region of a given sample at several beamlines such as ID21 and ID22/ID18F, special care is taken to develop sample holders that fit reproducibly at several beamlines.

A system of in-house-built encoded XYZ stages driven by stepper motors allow sample alignment and scanning over a range of 25 mm with a resolution of $\sim$100 nm with a positioning reproducibility of 100 nm. A Y-Z piezo nanopositioner and scanner (Physik Instrument) equipped with integrated capacitive sensors will soon be available for high-resolution scanning experiments providing $\sim$1 nm resolution within a 100 µm $\times$ 100 µm travel range.

Sample rotation for tomography measurements is performed using a MICOS rotation stage. Also an X translation, a tilt (for tomography) and a coarse rotation stage (for scanning XRF) are implemented at the base of the sample stage.

2.3.3. Detectors. Several types of detectors and beam monitors are available at the beamline corresponding to the needs of the different experimental techniques. The characteristic X-ray fluorescence line intensities of the sample are detected by a Si(Li) detector (Gresham Scientific Instruments) of active area 30 mm^2 and active thickness 4 mm, having an 8 µm-thick Be window. The energy resolution of the detector is 150 eV/Mn-$K\alpha$/FWHM at 4 µs shaping time. The Si(Li) detector is usually placed at 90° to the incoming linearly polarized X-ray beam in the storage beam plane in order to minimize the intensity of the scattered peaks in the spectra. The solid angle of detection and the detected scattered intensity can be optimized by using external collimators made from the stack of pure Al, Fe and Ta in order to avoid the appearance of spurious X-ray peaks in the spectra. The detector itself is placed onto motorized translation stages, allowing micrometer-range position optimization. A CANBERRA 2004 Amplifier, Canberra 8715 ADC and CANBERRA 556A AIM are used for collecting the XRF spectra. If needed, a Si drift-diode detector can also be installed at the beamline and the spectra of both detectors can be collected simultaneously.

The beamline will be equipped with a 13-element solid-state detector (Gresham Scientific Instruments) during the first half of 2005. The detector is composed of 13 separate Si(Li) crystals of active area 50 mm^2 and active thickness 4 mm, and will be arranged along a spherical surface allowing for optimal detection in the 30–70 mm sample–detector distance range. The multielement detector will be available for scanning

micro-XRF and micro-XAS experiments resulting in significantly increased data throughput.

In order to monitor the intensity of the incoming, focused and transmitted beam, different monitors such as ionization chambers or PIN diodes are used depending on the energy range.

For imaging/tomography experiments several high-resolution CCD cameras (Princeton Instruments TE/CCD-1242-EM/1, Sensicam QE, Photometrics, Frelon in the second experimental hutch) of different dynamic range and read-out speed are available at the beamline in order to fit to the needs of the experiment. The high-resolution cameras consist of a crystal scintillator (LAG, LAG:Eu, LAG:Tb, YAG) of thickness 3.5–26 µm depending on the required spatial resolution and detection efficiency, a light microscope optics with variable magnifications in the 10–40× range and a CCD chip. Spatial resolution of >1 µm with a field of view of 0.25–1 mm can be obtained by the appropriate combination of the scintillator and microscope optics. Exposure times as low as 5 ms can be achieved for time-resolved imaging experiments.

A Photonic Science CCD camera is used for microdiffraction experiments mostly in Laue geometry. It has a powder scintillator screen of diameter ∼7 cm with tapered fiber optics coupled to the CCD chip containing 1152×1242 pixels of physical pixel size 66.84 µm^2.

A videomicroscope of working distance 5.6 cm with a variable field of view in the 0.2 mm (V) × 0.26 mm (H) to 3.2 mm (V) × 4.16 mm (H) range and ∼1 µm maximum spatial resolution allows for the precise determination of the focal plane of the used focusing device and for the easy alignment of the sample.

3. Experimental techniques available at ID22

3.1. Scanning µ-XRF and XRF tomography

Scanning µ-XRF is a powerful technique for obtaining information about the spatial elemental distribution and elemental correlations on a (sub)micrometer scale. Owing to the high intensity ($1–5 \times 10^{11}$ photons s^{-1} in the case of KB) of the focused beam, ppm relative and fg absolute detection limits can be achieved in a measurement time of 1 s (see Fig. 3), making the study of trace-element distribution possible. X-ray fluorescence tomography provides the possibility for the non-destructive measurement of the quantitative internal elemental distribution of the sample (Golosio et al., 2003). By helical fluorescence tomography (Golosio et al., 2004) the measurement of the three-dimensional elemental concentration is also possible.

Scanning µ-XRF measurements can be performed in two different modes, either in step-by-step mode or in continuous motor movement (fast scan) mode. The full X-ray fluorescence spectrum (usually 2048 channels) is saved in each measured pixel independently of the scanning mode. The high intensity of the focused beam and the throughput of the Si(Li) detector (∼12 000 counts s^{-1} at 4 µs shaping time and 30% dead time) make the collection of spectra with sufficient

statistics and spectrum quality possible in 200 ms dwell time depending on the sample characteristics. The X-ray line intensities can be determined either by defining software regions of interest or by fitting each spectra 'online' using the AXIL software (Vekemans et al., 1994). The spectrum fitting makes the determination of the net peak intensities possible by taking into account the overlapping X-ray peaks and by subtracting the background.

3.2. Micro X-ray absorption spectrometry

The oxidation state and chemical speciation of a given element can be investigated by changing the energy of the excitation beam around its absorption edge (µ-XANES). In order to optimize the intensity variation of the incoming beam in the scanned energy range the change of the energy can be followed by the undulator gap. µ-XANES measurements can be performed either in transmission or in fluorescence mode. In the first case, Si photodiodes or ionization chambers filled with appropriate gas are used for monitoring the incoming (I_0) and transmitted beam intensity, while in fluorescence mode the Si(Li) detector is used for collecting the X-ray fluorescence signal. The use of the achromatic KB mirror provides the possibility of measuring the X-ray absorption spectra of several elements in the very same sample spot without realignment of the set-up. Various reference foils (EXAFS materials) are used for the calibration of the monochromator over a broad energy range.
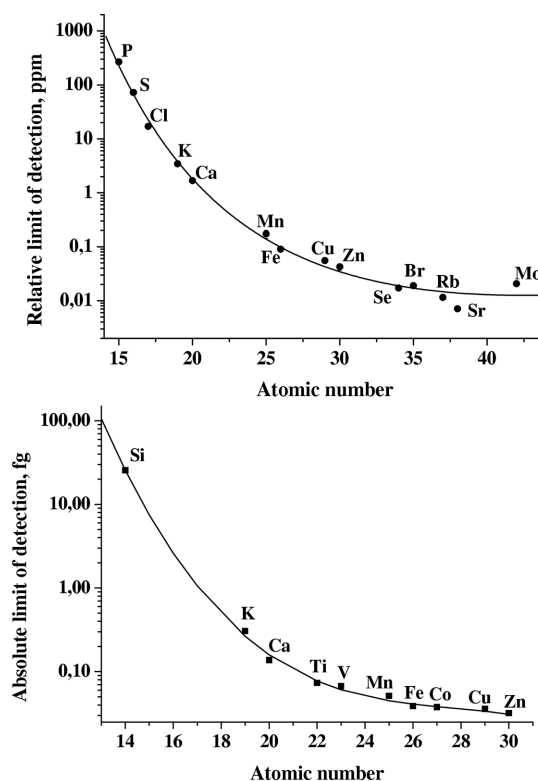

Figure 3
Relative and absolute limits of detection. Focusing device: KB mirror, spot size 0.8 µm (V) × 3.5 µm (H), live time 10 s, energy of the excitation beam 21 keV.

3.3. Scanning X-ray microdiffraction

By installing a two-dimensional diffraction camera after the sample in transmission mode, XRD patterns can be measured simultaneously with XRF spectra allowing for the simultaneous investigation of the crystalline structure and the elemental distribution. The diffraction camera is optimized along the beam in order to adjust the detected angular range to the requirements of the sample and the excitation energy. By varying the sample CCD distance, both wide- and small-angle X-ray scattering experiments can be carried out.

3.4. Imaging/tomography

The morphology and internal structure of the sample can be investigated by full-field X-ray absorption/phase-contrast imaging/tomography. Owing to the reproducible displacement of the KB mirror (and CRLs) these techniques can be combined with the above-mentioned X-ray microprobe techniques without the need of the realignment of the focusing device. Thus the investigation of the correlation between the morphology and other characteristics of the sample is possible. As an example, in Fig. 4 the three-dimensional volume rendering of the absorption tomography of a fluid inclusion

(a)

(b)

Figure 4
(a) Three-dimensional rendering of the reconstructed absorption tomography of an inclusion trapped in quartz material. (b) X-ray fluorescence spectra measured at the position of the inclusion fluid (light blue in the upper figure), the mineral with high metallic content (dark blue), the NaCl crystalline phase (yellow) and the gas phase (red).

(Cauzid *et al.*, 2004) is shown together with the XRF spectra measured in voxels containing different phases of the inclusion.

4. Scientific applications

The flexible beamline design together with the easy combination of different microprobe techniques makes the beamline attractive for several user communities. In the following, two examples from the field of material and environmental science will be presented to illustrate the technical possibilities of the beamline.

4.1. Mn-doped GaN

Electronics devices that apply the spin degree of freedom to perform their functions form the foundation of spintronics or magnetoelectronics. In particular, diluted magnetic semiconductors play an important role in the development of new spintronics devices, since producing semiconductor structures would make possible new ultrafast multifunctional electronics combining logic, non-volatile data storage and communication on a single chip. Mn impurities in GaN (GaN:Mn), for instance, introduce exceptional magnetic characteristics, with ferromagnetism even at room temperatures. However, the mechanism by which ferromagnetism is produced in this system, *e.g.* whether GaN with Mn clusters or random (Ga,Mn)N alloys are formed, is still not fully understood and requires the study of cluster formation and possible local atomic distortions around Mn sites.

In this study, molecular-beam-epitaxy-grown GaN doped with different Mn concentrations in the 0.07–13.7% range were investigated by scanning μ-XRF and μ-XANES (Martinez-Criado, Somogyi, Herman *et al.*, 2004). GaN:Mn layers of thickness 1 µm were deposited on an AlN nucleation layer grown on a (0001) sapphire substrate. By creating a horizontal secondary source by closing the beamline slits to 50 µm, a submicrometer resolution [0.6 µm (H) $\times$ 0.9 µm (V) spot-size] of $\sim 10^{10}$ photons s^{-1} intensity at 12 keV has been achieved. In order to study the cluster formation of Ga and Mn together with the possible appearance of other impurities, the samples were scanned in the focused beam while collecting the full XRF spectra at each sample point. The concentration of Mn in each pixel and the average Mn concentration in the GaN:Mn layer has been estimated from the measured Ga-$K\alpha$/Mn-$K\alpha$ intensity ratios taking into account the corresponding X-ray fluorescence yields. The sum of the Mn and GaN concentration was assumed to be 100% as no other elements/impurities could be detected in the XRF spectra. The samples with $\sim$0.07–2.34% Mn content showed homogeneous elemental distributions, while Mn and Ga clusters of several µm size could be detected for [Mn] $\simeq$ 13.7% Mn (see Fig. 5). The map of the Ga $K\alpha$, Mn $K\alpha$ and scattered intensity reveals the strong spatial correlation between the high-intensity Ga and Mn clusters.

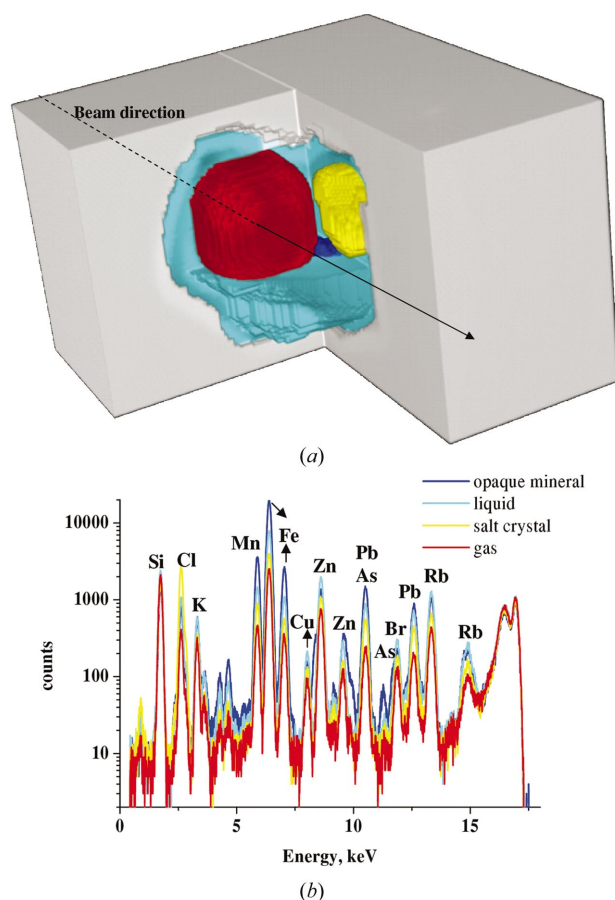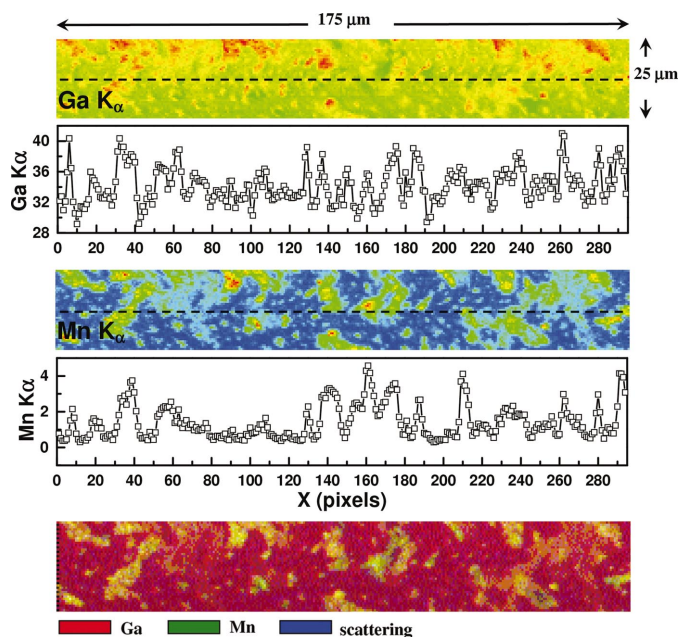XANES spectra of GaN as a function of the Mn content (see Fig. 6) have been measured in fluorescence mode at the

Figure 5
Ga and Mn distribution in the GaN:Mn sample of ∼13.7% Mn content. The profiles show the intensity change of Ga $K\alpha$ and Mn $K\alpha$ along the dashed lines indicated in the intensity maps. The lowest map shows the spatial correlation between Ga and Mn.
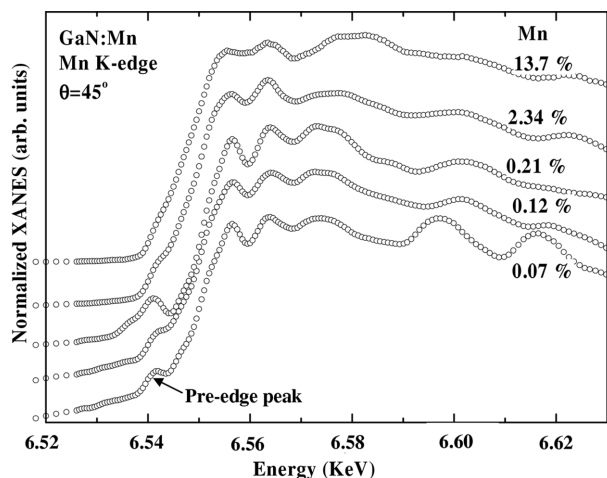

Figure 6
XANES spectra of the GaN samples doped with different Mn concentrations.

Mn K-edge in the 6496–6682 eV energy range with 0.5 eV energy steps. The measurements were performed at an incident angle of ∼45°. μ-XANES spectra measured at different locations of the samples containing 0.07–2.34% Mn did not show significant difference. For the highest Mn-doped samples the appearance of a pre-edge structure within the Mn-rich clusters could be detected (Martinez-Criado, Somogyi, Ramos *et al.*, 2004).

The relative intensities of the oscillations and the pre-edge regions of the XANES spectra are changing with varying Mn concentration. The observed Mn pre-edge peak indicates substitutional Mn incorporation into GaN, the contribution of

which is decreasing with increasing Mn concentration. This result, together with the smoothing and broadening of the oscillation features with increasing Mn concentration, indicates increasing short-range disorder around Mn with increasing Mn impurity content.

4.2. Investigation of the possible environmental impact of waste fly-ash material

The investigation of the environmental impact of waste fly ash necessitates the thorough study of its chemical properties in order to predict the possible chemical/environmental processes leading to leaching and biological uptake of the toxic trace metals and their compounds. The combination of different non-destructive X-ray microprobe techniques for the complex study of the heavy-metal distribution, concentration and speciation, together with the matrix composition and morphology within individual fly-ash particles, provides valuable complementary information to bulk analytical methods giving insight into the chemical processes happening at the single-particle [(sub)micrometer] level. Moreover, the investigation of individual particles is the only possible method of checking and developing theoretical models of the fly-ash-forming processes during combustion, which might lead to the improvement of the combustion procedure itself through a better control of the transport of heavy metals. In order to obtain statistically significant results, the study of a large number of particles is necessary.

The investigation of individual fly-ash particles was performed during several experimental runs at ID18F and ID22. For scanning μ-XRF the energy of the incoming beam was chosen to be 27 keV in order to excite the characteristic X-ray lines of heavy metals up to Cd. The beam was focused either by compound refractive lenses [CRL, spot-size 2 μm (V) × 6 μm (H)] or by the KB mirror used at 2 mrad incident angles [spot size 2 μm (V) × 4 μm (H)]. The results are detailed in several publications (*e.g.* Camerani *et al.*, 2001; Camerani-Pinzani *et al.*, 2002, 2004); thus only a brief description is given here for illustrating the technical possibilities of the beamline.

In order to investigate the spatial elemental distribution and inter-elemental correlation within single particles and the dependence of the heavy-metal content on the particle size, several particles of different sizes were raster scanned in the focused beam while registering the XRF spectra in each voxel. Since fly-ash particles usually contain a large number of detectable elements with overlapping X-ray lines (see the average spectrum in Fig. 7a) the measured X-ray spectra of the pixels were fitted using the *AXIL* software. The precise quantification of the elemental content is usually not possible only from a two-dimensional scan owing to the unknown sample morphology and matrix composition. On the other hand, semi-quantitative concentrations in each measured voxel can be obtained (neglecting the self-absorption within the particle) by registering the transmitted signal and using the matrix composition known from bulk measurements. This semi-quantitative approximation can give a valuable estima-
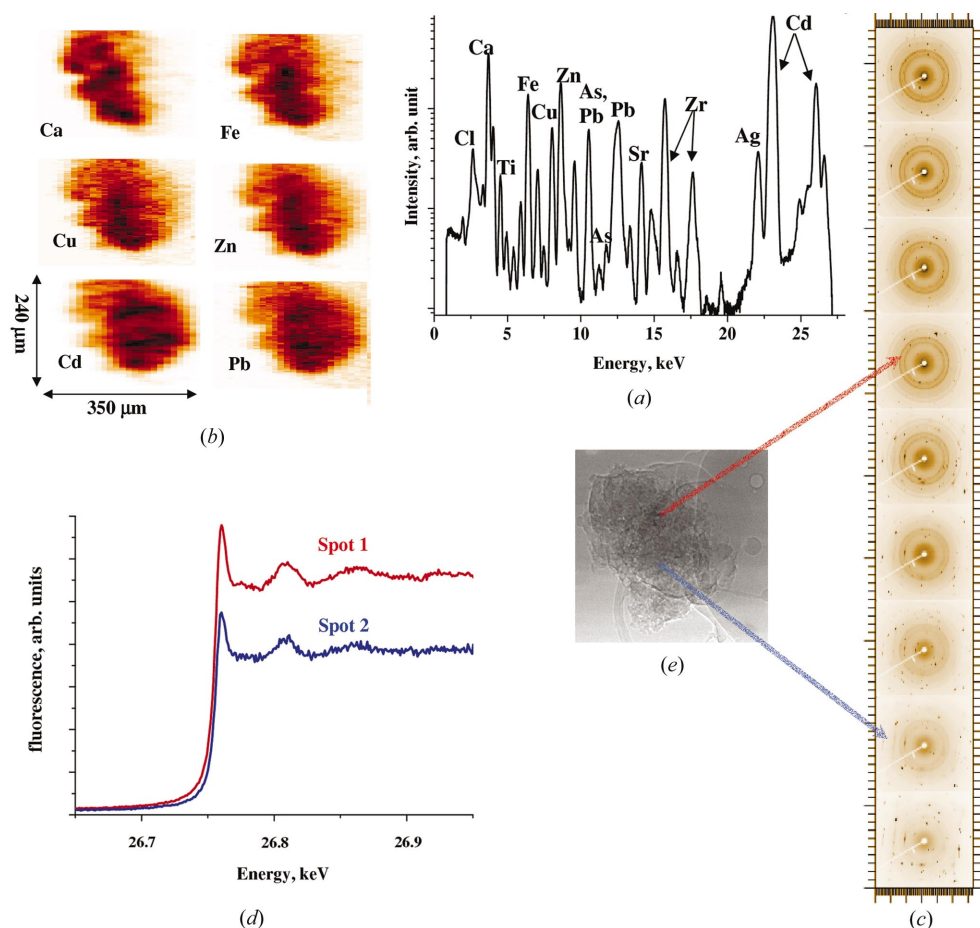
Figure 7
Investigation of a single waste fly-ash particle by combined X-ray microprobe techniques: (*a*) average XRF spectrum of the particle, (*b*) elemental distribution maps obtained from scanning μ-XRF, (*c*) scanning μ-XRD, (*d*) μ-XANES, (*e*) absorption projection.
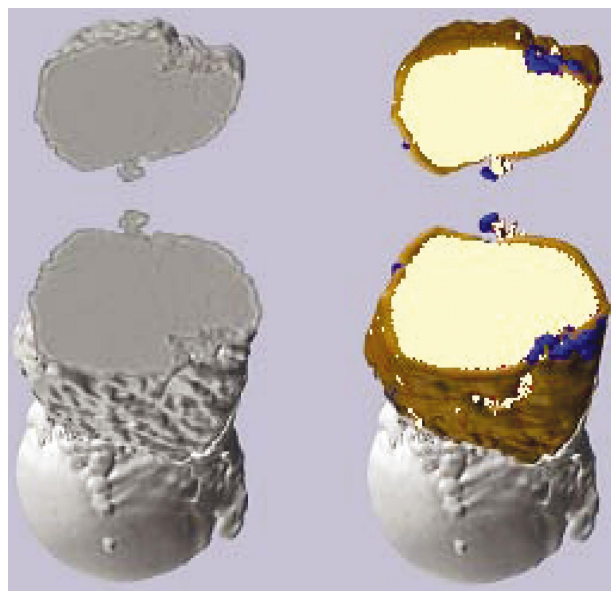

Figure 8
Three-dimensional rendering of conventional transmission tomography (left) and of the distribution of rubidium (yellow), manganese (brown) and iron (blue) obtained by helical fluorescence tomography. The sample is glued on the top of a silica capillary, which is partly visible at the lower part of the images.

tion of the heavy-metal content of a statistically significant number of particles, which is crucial for the estimation of the harmfulness of the fly-ash material.

The possible fate of heavy metals is also influenced by their position within the particle: on the surface they are most prone to leaching while at some depth within the matrix they might be more shielded from chemical attack from, for example, rain water. Owing to the large penetration depth of high-energy X-rays, the two-dimensional elemental maps (see Fig. 7*b*) only reflect the variation of the overall concentration among the irradiated voxels but do not give any information about the internal elemental distribution. The internal elemental distributions can be reconstructed by appropriate mathematical algorithms from X-ray sinograms obtained by successive linear scans and rotations of a slice of the sample (X-ray fluorescence tomography). In order to obtain information about the morphology (three-dimensional linear absorption coefficient distribution) of the particle, usually determined by the light non-detectable elements, X-ray absorption tomography can be utilized by registering the absorption projection of the sample in the full beam by a high-resolution CCD camera (see Fig. 8). For obtaining precise quantitative internal elemental distributions, a new non-destructive X-ray technique has been developed at ID22 by combining simultaneous transmission, fluorescence and Compton microtomography (Golosio *et al.*, 2003). The combination of the fast-scan technique and the helical scan of the sample makes a full three-dimensional combined XRF/Compton/transmission tomography possible within some ($\sim$8) hours. In Fig. 8 the distributions of Rb, Mn and Fe within a fly-ash particle are shown as an example. The combined helical tomography (Golosio *et al.*, 2004) reveals that the external layer of the particle has different elemental composition than its inner part. The presence of a fragmented part with higher iron concentration can also be distinguished. These observations provide unique information about the possible fly-ash formation mechanisms (*e.g.* volatilization, condensation, diffusion, solid solution formation) during combustion. Although the above-mentioned X-ray fluorescence and combined tomographic techniques are relatively time-consuming, making them less suitable for the analysis of large

numbers of particles, they provide unique information about the internal structure of particles pre-selected from scanning XRF measurements.

The variation of the crystalline structure of the matrix can be a valuable tool for the study of the possible attachment of the investigated elements to a given crystalline structure. As shown in Fig. 7(c), the XRD spectra of the particles can be measured in each voxel simultaneously with their XRF spectra.

The prediction of the dissolution and transport of different metal compounds from the ash matrix to soil water is a key step when investigating the environmental effect of ash material since dissolved compounds are available for biological uptake and ground-water contamination. Thus the toxicity of ashes strongly depends on the chemical speciation of the different potentially toxic elements. The chemical speciation of a given element in a voxel chosen on the basis of the two-dimensional XRF/XRD maps can be investigated by μ-XAS. The extended XANES spectra of the element to be investigated (see Fig. 7d) can be obtained either in fluorescence or absorption mode depending on its concentration. In our study, the XANES of Cd, having some tens of ppm concentration, has been investigated in fluorescence mode. Comparisons of XAS spectra between fly ashes and reference compounds suggest that in the particles studied Cd is present in the oxidation state +2 and is an admixture of $CdSiO_3$ and the leachable CdO, $CdCl_2$. On the other hand, X-ray fluorescence tomography showed that Cd was distributed not only on the surface but also within the matrix of the investigated slices, thus 'hidden' from the direct dissolution of the rain/etc. water.

From an environmental perspective, these results are of particular importance when considering the possible short-term leaching potential of the fly ashes. It is expected that knowledge of the spatial elemental distribution, crystalline structure and speciation of different heavy metals, as obtained in the present study for Cd, would allow formulation of models for the formation of fly-ash particles during the combustion process. These models may be used as a basis to improve combustion processes by including the control of the transport of heavy metals.

5. Summary and conclusion

The flexible experimental design of the ID22 hard X-ray microprobe beamline makes possible the combined use of different microanalysis techniques, such as μ-XRF, μ-XRD, μ-XAS and μ-imaging/tomography. Various sample environments, such as high-pressure cells, helium chambers and cryo-cooling, can be included into the set-up. The high photon flux together with the large data throughput and adapted (fast/varying scanning limits) scanning possibilities makes the measurement of large numbers of samples possible during the time frame (some days) of a standard user experiment. This also ensures that two-dimensional/three-dimensional fluorescence or combined XRF/Compton/absorption tomography can be offered as a standard technique for the user community

of the beamline. Online data treatment facilitates the follow up of the measurements during the experiment. These possibilities make ID22 well adapted to the needs of several research fields such as biology, geology, environmental science and material science as is illustrated by the chosen scientific examples.

References

Camerani, M. C., Somogyi, A., Drakopoulos, M. & Steenari, B. M. (2001). *Spectrochim. Acta B*, **56**, 1355–1356.

Camerani-Pinzani, M. C., Ansell, S., Somogyi, A., Steenari, B. M. & Lindquist, O. (2004). *Anal. Chem.* **76**, 1596–1602.

Camerani-Pinzani, M. C., Somogyi, A., Simionovici, A., Ansell, S., Steenari, B. M. & Lindquist, O. (2002). *Environ. Sci. Technol.* **36**, 3165–3169.

Cauzid, J., Philippot, P., Somogyi, A., Simionovici, A., Bleuet, P. & Ménez, B. (2004). *Anal. Chem.* **76**, 3988–3994.

Chubar, O. & Elleaume, P. (1998). *Proceedings of the EPAC98 Conference*, Stockholm, pp. 1177–1179.

David, C., Nöhammer, B. & Ziegler, E. (2001). *Appl. Phys. Lett.* **79**, 1088–1090.

Golosio, B., Simionovici, A., Somogyi, A., Lemelle, L., Chukalina, M. & Brunetti, A. (2003). *J. Appl. Phys.* **94**, 145–156.

Golosio, B., Somogyi, A., Simionovici, A., Bleuet, P., Susini, J. & Lemelle, L. (2004). *Appl. Phys. Lett.* **84**, 2199–2201.

Hignette, O., Rostaing, G., Cloetens, P., Rommeveaux, A., Ludwig, W. & Freund, A. (2001). *Proc. SPIE*, **4499**, 105–116.

Lengeler, B., Schroer, C. G., Benner, B., Gerhardus, A., Günzler, T. F., Kuhlmann, M., Meyer, J. & Zimprich, C. (2002). *J. Synchrotron Rad.* **9**, 119–124.

Lengeler, B., Schroer, C. G., Kuhlmann, M., Benner, B., Günzler, T. F., Kurapova, O., Somogyi, A., Snigirev, A. & Snigireva, I. (2004). *AIP Conf. Proc.* **705**, 748–751.

Marcus, M. A., MacDowell, A. A., Celestre, R., Manceau, A., Miller, T., Padmore, H. A. & Sublett, R. E. (2004). *J. Synchrotron Rad.* **11**, 239–247.

Martinez-Criado, G., Somogyi, A., Hermann, M., Eickhoff, M. & Stutzmann, M. (2004). *Jpn. J. Appl. Phys.* **43**, L695–697.

Martinez-Criado, G., Somogyi, A., Ramos, S., Campo, J., Tucoulou, R., Salome, M., Susini, J. & Stutzmann, M. (2004). *Appl. Phys. Lett.* Accepted for publication.

Nazmov, V., Reznikova, E., Boerner, M., Mohr, J., Saile, V., Snigirev, A., Snigireva, I., DiMichiel, M., Drakopoulos, M., Simon, R. & Grigoriev, M. (2004). *AIP Conf. Proc.* **705**, 752–755.

Newville, M., Sutton, S., Rivers, M. & Eng, P. (1999). *J. Synchrotron Rad.* **6**, 353–355.

Schroer, C. G., Kuhlmann, M., Hunger, U. T., Günzler, T. F., Kurapova, O., Feste, S., Frehse, F., Lengeler, B., Drakopoulos, M., Somogyi, A., Simionovici, A. S., Snigirev, A., Snigireva, I., Schug, C. & Schröder, W. H. (2003). *Appl. Phys. Lett.* **82**, 1485–1487.

Sutton, S. R., Newville, M., Eng, R., Rivers, M. & Lanzirotti, A. (2004). *Adv. X-ray Anal.* **47**. In the press.

Vekemans, B., Janssens, K., Vincze, L., Adams, F. & VanEspen, P. (1994). *X-ray Spectrom.* **23**, 278–285.